







Coupling SMAP Brightness Temperature Into SWAT Hydrological Model for 30-m Resolution Soil Moisture Retrievals

Luyao Zhu , Junyu Qi , Hongquan Wang , Mengmeng Zhou, Yang Ye , Yongjun Li, Cheng Tong , Xiaodong Deng , Shan He, and Ke Wang, *Member, IEEE*

Abstract—Integrating satellite observations into hydrologic models has the potential to enhance soil moisture (SM) retrievals at high spatial and temporal resolutions. The hydrological model Soil and Water Assessment Tool (SWAT) can produce spatiotemporally continuous SM product with high resolution. This article proposed to physically couple the SWAT and *Tau-omega* radiative transfer model to retrieve SM with a spatial resolution of 30 m. First, the SWAT model integrated a physically based SM module used to simulate hourly SM, from which the brightness temperature (*TB*) at 30 m was obtained by forwardly simulating the *Tau-omega* model. Then, the simulated *TB* at fine resolution and Soil Moisture Active and Passive (SMAP) *TB* at coarse resolution were merged by Kalman filter into a disaggregated *TB*. Finally, SM at 30 m resolution was retrieved from the disaggregated *TB*. The proposed methods were evaluated over the Lanjiang River Basin. The results show that the retrieved SM is highly correlated with two official SMAP SM products and that it has a better accuracy than five SMAP SM products. Particularly, due to the high resolution, the retrieved product captured the heterogeneity of SM within and among fields, compared to the individual use of the hydrological model or satellite observation. Our proposed approach can aid the decision-making in agricultural management at the field scale.

Index Terms—Brightness temperature (*TB*), high spatial resolution, soil moisture (SM), Soil Moisture Active and Passive (SMAP), Soil and Water Assessment Tool (SWAT), *Tau-omega* model.

I. INTRODUCTION

SOIL moisture (SM) is critical for land–atmosphere interaction, terrestrial ecosystem, and carbon uptake [1], [2],

Manuscript received 2 January 2023; revised 17 August 2023; accepted 25 August 2023. Date of publication 30 August 2023; date of current version 18 September 2023. This work was supported by the National Natural Science Foundation of China under Grant 32171781 and Grant 42001201. (*Corresponding author: Hongquan Wang.*)

Luyao Zhu, Hongquan Wang, Yongjun Li, Cheng Tong, Xiaodong Deng, and Ke Wang are with the College of Environmental and Resource Sciences, Zhejiang University, Hangzhou 310058, China (e-mail: luyao_zhu@zju.edu.cn; hongquan.wang@usherbrooke.ca; yongjunli@zju.edu.cn; 21714124@zju.edu.cn; xddeng@zju.edu.cn; kwang@zju.edu.cn).

Junyu Qi is with the Earth System Science Interdisciplinary Center, University of Maryland, College Park, MD 20740 USA (e-mail: junyuqi@umd.edu).

Mengmeng Zhou is with the College of Business, Changzhou University, Changzhou 213164, China (e-mail: mm_zhou2022@163.com).

Yang Ye is with the College of Spatial Planning and Design, Zhejiang University City College, Hangzhou 310015, China (e-mail: yangye1993@zju.edu.cn).

Shan He is with the College of Economics and Management, China Jiliang University, Hangzhou 310029, China (e-mail: heshan33@cjlu.edu.cn).

Digital Object Identifier 10.1109/JSTARS.2023.3310197

[3], [4]. High spatial resolution SM contributes to precision agriculture, water resource management, and the simulation of land surface, crop, and hydrological models [5], [6], [7].

Due to the influence of precipitation, soil texture, vegetation growth, and topography, surface SM has complex spatial heterogeneity and temporal variability. Traditional in-situ measurements only represent changes in SM at the point scale. Conversely, remote sensing provides an effective tool to monitor SM at different spatiotemporal scales. Compared with visible and thermal infrared bands, microwaves with longer wavelengths (1 mm–1 m) can work under all-day and all-weather conditions, and have the ability to penetrate vegetation and topsoil [8]. Microwave remote sensing comprises active and passive types. Synthetic aperture radar (SAR) in active type has high spatial resolution, but its signal is strongly impacted by surface roughness, vegetation biomass, and canopy structure, leading to high retrieval uncertainty. In addition, speckle effects and other complex data processing problems hindered the application of SAR [9].

In contrast, passive brightness temperature (*TB*) is less influenced by surface roughness and vegetation characteristics. Among passive microwaves, the low-frequency *L*-band (1–3 GHz) radiometer such as Soil Moisture and Ocean Salinity (SMOS) [10] and Soil Moisture Active and Passive (SMAP) [11] is currently the best band for detecting surface SM [12], [13]. Compared to SMOS, the SMAP *TB* has the advantage of excellent radio frequency interference corrections [9]. Therefore, our study used the *TB* and SM data from SMAP mission. Nevertheless, due to coarse spatial resolution of about tens of kilometers, the passive microwave SM products failed to capture spatial heterogeneity of SM at field scale. Consequently, it is important to develop disaggregation algorithms for SM retrievals with high spatial resolution and broad coverages, which can better serve the agricultural irrigation, crops disaster monitoring, and drought/inundation management.

The basic theory of disaggregation algorithms is to establish relationships between remote sensing products and ancillary geophysical observations (vegetation and soil properties). For SM, there are following three types of disaggregation algorithms [14].

- 1) Multisource data fusion algorithm, but it is limited by the low revisit rates of radar [15] and the contamination of optical data by cloud [16].

- 2) Geographic information-based algorithm, which assumes that SM depends on topography, soil attributes, and vegetation characteristics [17], but it requires a large number of site observations.
- 3) Model-based algorithm, which mainly includes statistical [18] and hydrological models [19].

Different from other disaggregation methods, the hydrological models driven by meteorological data account for the interaction between land and atmosphere, and meteorological factors such as precipitation and temperature have a significant impact on SM. Based on solid physical processes and dynamic mechanisms, the hydrological models can clearly depict the interactions between each component in the water cycle, and simulate the SM continuously in the temporal and spatial dimensions.

In recent years, the Soil and Water Assessment Tool (SWAT) model has been extensively used because of its robust physical mechanisms, simple inputs, and good performance. SWAT takes hydrologic response unit (HRU) as the basic analysis unit, by fully taking into account the land use, soil, topography, and meteorological attributes to quantify the hydrological process [20], [21], [22], [23], [24]. Narasimhan et al. [25] obtained long-term SM dataset by SWAT, which was well correlated with vegetation growth. Mengistu et al. [26] and Havrylenko et al. [27] applied the SWAT model to the South African and Pampas region, respectively, indicating that the simulated SM can reasonably assess agricultural drought. Li et al. [28] showed that the SWAT simulated SM captured SM trends at various soil depths and time scales, and the temporal variability of surface SM best matched the in-situ values. In summary, the ability of SWAT model was validated in simulating SM variations and trends. However, it employs a simple bucket module for depicting the movement of SM leads to some limitations in precisely characterizing SM [28], [29]. Furthermore, it should be noted that satellite data provide SM information at a specific moment, whereas the original SWAT model is designed to generate SM values at a daily scale and lacks the capability to simulate hourly SM. Therefore, this study introduced a SWAT model based on the Richards equation (RSWAT) to simulate hourly SM [30], subsequently the simulated SM data are utilized to disaggregate the SMAP data.

In addition, the satellite retrieved SM is not consistent with the model simulated SM because they used different algorithms and auxiliary data [31], [32]. The direct combination of satellite SM data with the SWAT model may lead to a significant uncertainty. Consequently, this study combined the RSWAT model with SMAP *TB* data rather than SM data to reduce uncertainty. Within this context, we proposed to disaggregate SMAP *TB* data from 36 km to 30 m at basin scale by coupling the RSWAT model with radiative transfer model (RTM) [33]. Subsequently, SM at 30 m spatial resolution was retrieved from disaggregated *TB* by using the RTM. This approach is physically explanatory and transferable to other regions. Especially, most disaggregation studies of SMAP only obtained 1 km SM due to the limitation of coarse-resolution auxiliary data [34], [35], [36]. Disaggregation based on the RSWAT model can produce SM product with 30 m

spatial resolution, which benefits the practical applications such as selective irrigation at the field scale.

II. STUDY AREA AND DATASETS

A. Study Area

The study area is the Lanjiang River basin, which is in the southwestern part of Zhejiang Province, China. It is the main tributary of the Qiantang River Basin, and has a humid subtropical monsoon climate, with an average annual precipitation of approximately 1200–1700 mm and an annual average temperature of about 17 °C–18 °C [37]. The largest proportion of land cover type in the study area is forest, followed by cropland. As shown in Fig. 1, the overall terrain of the basin is characterized by a high surrounding and low center. The boxes with dashed black lines represent the SMAP 36 km grids, and the black dots mark the locations of the ground measurement stations.

B. Datasets

This study utilized three types of data, as listed in Table I for their details. Specifically, the data contained: 1) data for SWAT, including digital elevation model (DEM), land use, soil, and meteorological data; 2) data for RTM, including SMAP *TB*, land cover, normalized difference vegetation index (NDVI) products; 3) data for analysis, including in-situ SM observations, five SMAP products with different resolutions or algorithms (SAMP 36 km, enhanced 9 km, multichannel collaborative algorithm (MCCA), multitemporal dual channel algorithm (MT-DCA), and SMAP-IB), and ESA CCI active SM product.

1) *Data for SWAT Model*: DEM was from the NASA SRTM DEM with a resolution of 1 arc second [38], which was filled in this study. The filled DEM is more suitable for SWAT delineation of the watershed.

Land use products at 30 m resolution for 2015 were produced by the Department of Environmental Protection of Zhejiang Province. The study area initially contained 26 land use types, which were reclassified into 13 categories based on the SWAT classification code.

Soil data with a 30 arc seconds resolution was acquired from the Harmonized World Soil Database (HWSD) [39]. The soil properties database for SWAT was calculated by the Soil Water Characteristics Tool.

Meteorological data were obtained from the China Meteorological Administration (CMA), including precipitation, maximum and minimum temperatures, wind speed, relative humidity, and short-wave radiation. To attain SM at an hourly scale, this study used hourly precipitation, and the other elements are on a daily scale.

2) *Data for RTM*: The SMAP mission with an *L*-band radiometer and radar began operating in April 2015 [11], whereas radar was no longer produced active product after the high-power amplifier experienced an anomaly on July 7, 2015. Therefore, only the *L*-band radiometer data were available, which were collected at local overpass time of 6:00 A.M. for descending orbit and 6:00 P.M. for ascending orbit, respectively. Considering that

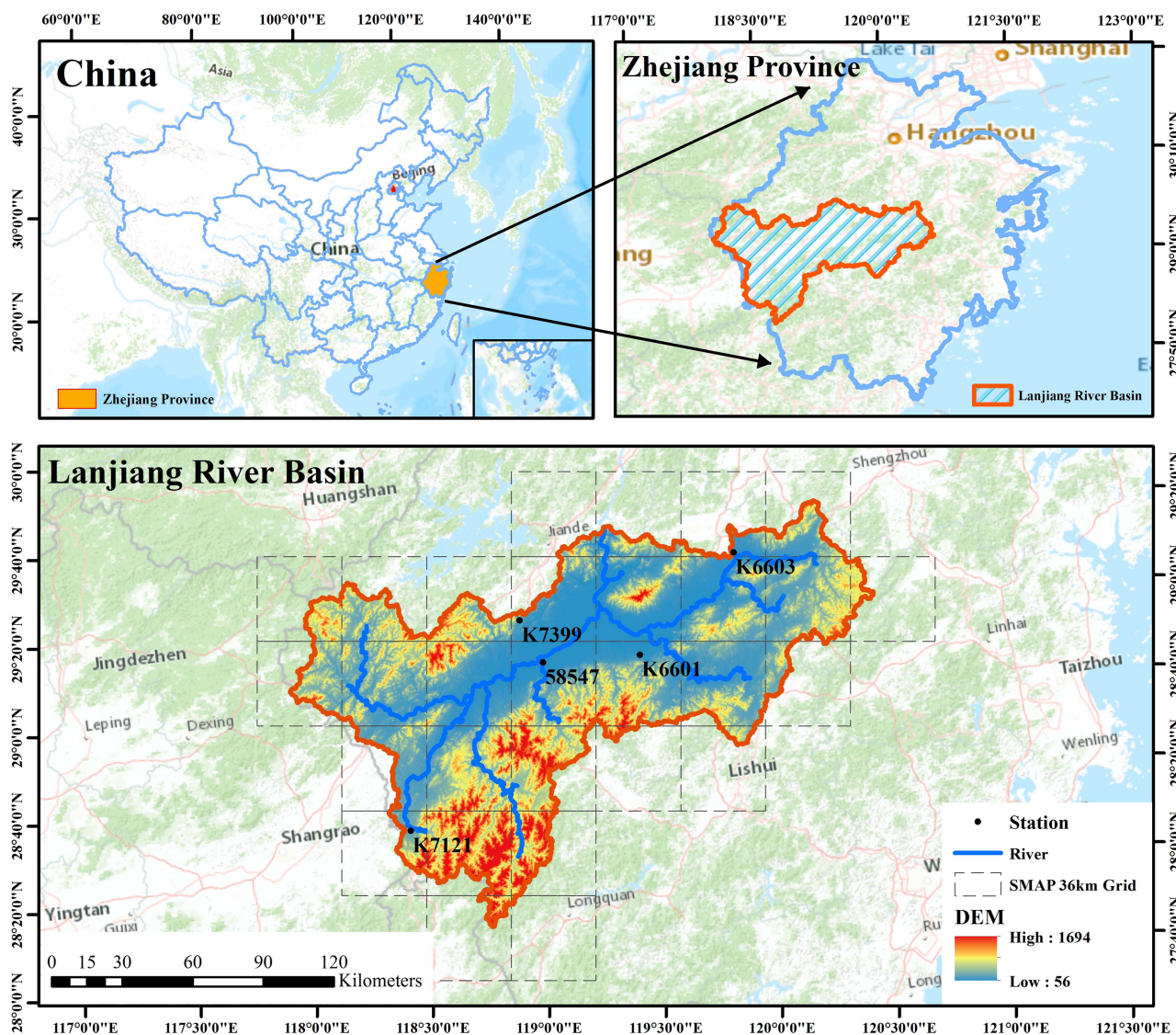


Fig. 1. Study area over Lanjiang River Basin, with locations of SMAP 36 km grids (dashed black boxes) and in-situ stations (black dots).

TABLE I
CHARACTERISTICS OF DATASETS USED FOR DRIVING SWAT, RTM, AND ANALYZING SPATIOTEMPORAL FEATURES

Type	Product	Variable	Spatial Resolution	Temporal Resolution	Period
Data for SWAT	<i>In-situ</i> data	Meteorological	Point-scale	Daily and Hourly	2017–2018
	Landuse	Landuse	30 m	Yearly	2015
	HWSD	Soil	30 arc seconds	—	—
	NASA SRTM DEM	DEM	1 arc seconds	—	—
Data for RTM	SMAP L3	<i>T_B</i>	36 km	Daily	2018
	MCD12Q1	Land Cover	1 km	Yearly	2018
	MOD13Q1 and MYD13Q1	NDVI	250 m	16-day	2018
Data for analysis	SMAP L3	SM	36 km	Daily	2018
	SMAP Enhance L3	SM	9 km	Daily	2018
	SMAP MCCA	SM	36 km	Daily	2018
	SMAP MT-DCA	SM	36 km	Daily	2018
	SMAP-IB	SM	36 km	Daily	2018
	<i>In-situ</i> data	SM	Point-scale	Hourly	2018
	ESA CCI active	SM	25 km	Daily	2018

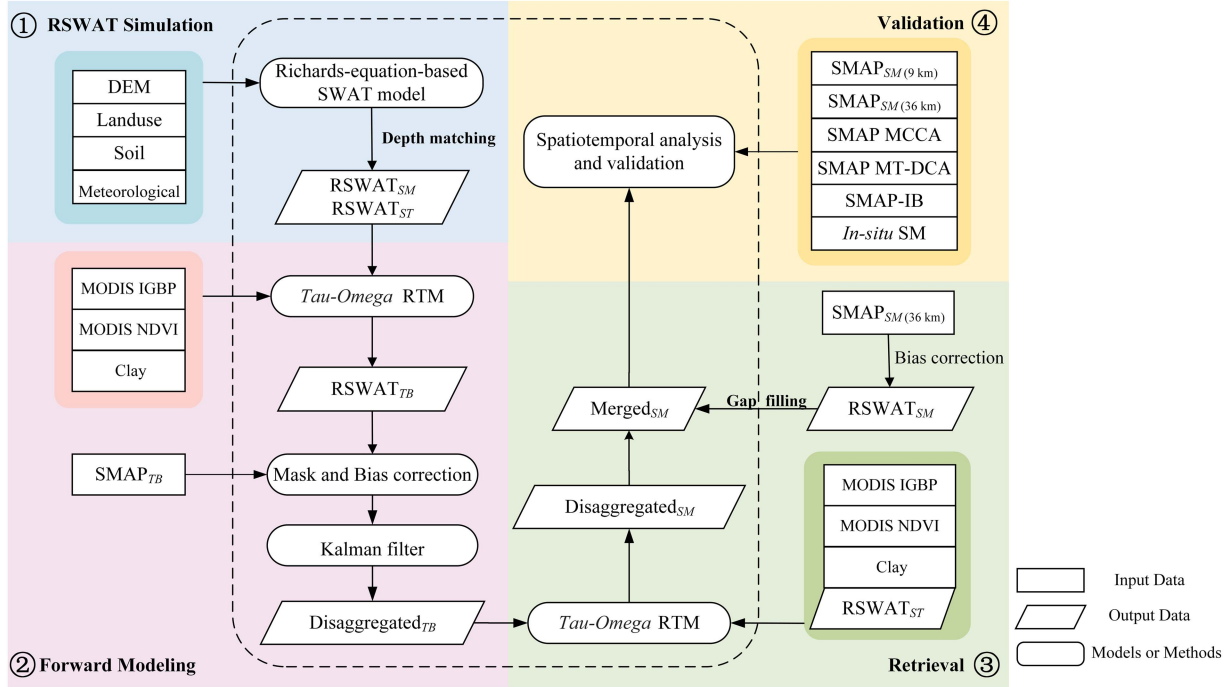


Fig. 2. Schematic diagram of the coupling method to obtain high spatial resolution (30 m) SM by combining RSWAT hydrological model, *Tau-omega* RTM, and Kalman filter.

the vertical distribution of surface and vegetation temperatures is more homogeneous in the morning than in the evening [40], the quality of descending SMAP data is usually better than the ascending [41]. Additionally, compared to horizontal polarization, *TB* at vertical polarization (*v-pol*) has better sensitivity to SM at top soil layer (5 cm) [42], [43]. Consequently, the SMAP 36 km *v-pol TB* product (SPL3SMP, Version 7) at 6:00 A.M. was selected.

Land cover data was obtained from Moderate Resolution Imaging Spectroradiometer (MODIS) land cover type products (MCD12Q1) in 2018, and we selected the IGBP classification scheme to identify the land cover type of pixels. According to the look-up table of the SMAP algorithm [44], the land cover data was used to determine vegetation structure and surface roughness parameters to drive the RTM.

The NDVI products used in this study consist of NDVI products from MODIS Terra and Aqua (MOD13Q1 and MYD13Q1), which are 16-day composites obtained by selecting high-quality surface reflectance pixels. The combination of these two products can further produce NDVI data at eight-day intervals, which were applied to calculate vegetation water content (VWC) parameter in RTM.

3) *Data for Analysis*: The in-situ SM observations were derived from the automatic soil moisture observation stations established by the CMA. These stations primarily employ three types of observation instruments: DNZ1, DNZ2, and DNZ3. The operating principles of these instruments are based on frequency reflection methods. Specifically, DNZ1 utilizes the standing wave method, whereas DNZ2 and DNZ3 utilize the capacitance method. The data were vertically stratified into eight different

depths (0–10 cm, 10–20 cm, 20–30 cm, 30–40 cm, 40–50 cm, 50–60 cm, 70–80 cm, and 90–100 cm) and recorded hourly. Within the study area, there are five available stations, and data in the 0–10 cm depth were selected to match the probing depth of the satellite (see Fig. 1). In addition, three state-of-the-art SM products were added for accuracy comparison, namely SMAP-MCCA [45], MT-DCA [46], and SMAP-IB [47].

SMAP 36 km and 9 km SM products [48] were used for spatial analysis. Compared to the 36 km SM product, 9 km product enhanced spatial detail and achieved satisfactory accuracy [49].

ESA CCI active SM product [50] was used to estimate the relative error of RSWAT SM and SMAP SM by triple collocation method.

III. METHODOLOGY

Fig. 2 illustrates the SM retrieval method proposed in this study. First, a Richards-equation-based SM module was integrated within the SWAT model to generate 5 cm SM and soil temperature at 6 A.M., and forward simulated RSWAT *TB* data at 30 m by *Tau-omega* RTM with MODIS and soil property data. Then, based on the RSWAT *TB*, the Kalman filter was employed to disaggregate SMAP *TB* data from 36 km to 30 m. Finally, the 30 m SM was retrieved by the RTM.

A. Simulate SM by RSWAT Model

The water balance equation is the foundation of the SWAT hydrological model

$$SW_t = SW_0 + \sum_{i=1}^t (P_{day,i} - Q_{surf,i} - ET_{a,i} - W_{weep,i} - Q_{gw,i}) \quad (1)$$

where t stands for time, SW_0 and SW_t represent soil water content at the beginning and end of the i th day, respectively, and $P_{day,i}$, $Q_{surf,i}$, $ET_{a,i}$, $W_{weep,i}$, and $Q_{gw,i}$ represent the precipitation, surface runoff, evaporation, soil profile recharge to groundwater, and return flow on the i th day, respectively. Their units are all in mm H₂O.

In the simulation of the SWAT model [51], the flow path characteristics of the DEM were first analyzed, based on which the watershed was divided into several subbasins. Then, these subbasins were further classified into HRUs according to the underlying surface conditions such as land use and soil type. Next, the meteorological data were used to drive model. Ultimately, the SWAT model formed a catchment area of 18 740 km² (see Fig. 1), and the whole basin was divided into 26 subbasins and 12 068 HRUs.

In addition, as this study combined SWAT simulated SM with SMAP data that penetrated to a depth of about 5 cm in units of volumetric moisture content (m³/m³), the SM simulated by the SWAT model had to be matched to SMAP in depth and units. For depth, this study weighted the SM and temperature of SWAT in the vertical direction to obtain data at 5 cm. For units, SWAT simulated SM as the value after removing the wilting point [51], and units are expressed in terms of water layer thickness (mmH₂O). Therefore, we first added the simulated SM to the wilting point value and divided by the soil thickness (mm) to obtain the volumetric moisture content.

Since the SMAP data at 6 A.M. was chosen for this study, in order to align with the acquisition time of SMAP and improve the accuracy of the simulation, the RSWAT model developed by Qi et al. [30] was adopted in this study. In comparison to the original SWAT model, RSWAT incorporated a physically based SM module based on the Richards equation, instead of the traditional bucket-based SM module. The Richards equation is employed in capturing and simulating water distribution and movement in three-dimensional space, considering factors such as soil porosity, infiltration, and soil characteristics. This equation enables a more precise depiction of SM dynamics across different soil layers. More importantly, RSWAT exhibits the capability to simulate moisture and temperature variations at an hourly resolution. For more detailed information on the RSWAT model, please refer to Qi et al. [30]. In this study, we used 30 m soil temperature and SM data at 6 A.M. each day in 2018 simulated by the RSWAT model.

B. Simulate RSWAT TB Using Tau-Omega Model

The *Tau-omega* model was used to obtain RSWAT TB from RSWAT SM. At L -band, this model ignores the effects of multiple scattering in the atmosphere and vegetation layers. TB consists of the following components: soil radiation after canopy attenuation, direct vegetation radiation, and radiation

from vegetation reflected by soil and attenuated by the canopy. Consequently, TB is modeled as

$$RSWAT_{TB} = T_{soil} \varepsilon_{soil} \gamma + T_{veg} (1 - \omega) (1 - \gamma) + T_{veg} (1 - \varepsilon_{soil}) (1 - \omega) (1 - \gamma) \gamma \quad (2)$$

$$\gamma = e^{-\tau / \cos(\theta)}$$

where T_{soil} and T_{veg} are soil temperature and vegetation effective temperature, respectively. At 6:00 A.M., we suppose that soil and vegetation temperatures are homogeneous under thermal equilibrium conditions, and T_{soil} is obtained from the SWAT model. ω is the single scattering albedo, γ represents transmissivity, which is simulated with the incidence angle (θ) of SMAP and vegetation optical depth (τ).

There is a linear relationship between τ and VWC [52]

$$\tau = (b \cdot VWC) / \cos(\theta) \quad \text{with}$$

$$VWC = (1.9134 \cdot NDVI^2 - 0.3215 \cdot NDVI) + stem_factor \cdot \frac{NDVI_{max} - NDVI_{min}}{1 - NDVI_{min}} \quad (3)$$

where NDVI is acquired from the MODIS NDVI product, $NDVI_{max}$ and $NDVI_{min}$ represent the maximum and minimum values of the NDVI during the study period, $stem_factor$ is the peak value of stem water content, and the constant b represents the vegetation parameter. $stem_factor$, b , and ω are related to the MODIS IGBP land cover type, and their value can be obtained from the land cover look-up table in SMAP algorithm documentation [44].

Now, the only unknown parameter left in (2) is soil emissivity (ε_{soil}), which is calculated as follows: first, RSWAT SM is converted to soil dielectric constant (ε_r) by Mironov dielectric model, which considers the difference between bound and free water in the soil layer. It is more suitable for the SM retrieval of L -band, the detailed formula for the model is described in [53]. Then, ε_r was transformed into smooth surface reflectivity (r_v) by the Fresnel coefficient equation [54]

$$r_v = \left| \frac{\varepsilon_r \cos(\theta) - \sqrt{\varepsilon_r - \sin^2(\theta)}}{\varepsilon_r \cos(\theta) + \sqrt{\varepsilon_r - \sin^2(\theta)}} \right|^2 \quad (4)$$

Next, the HQN roughness model [55] was adopted to convert r_v into the reflectivity of the rough surface (r)

$$r = r_v \cdot \exp(-h \cdot \cos^2(\theta)) \quad (5)$$

where h is an effective roughness parameter related to land cover types.

Finally, the soil emissivity was obtained from r

$$\varepsilon_{soil} = 1 - r. \quad (6)$$

Therefore, the 30 m RSWAT TB data can be derived from RSWAT SM by the *Tau-omega* model. The next step is to disaggregate the SMAP TB by RSWAT TB.

C. Disaggregate SMAP TB With RSWAT TB

1) *Bias Correction*: Due to factors such as spatial resolution, there exists a certain systematic bias between satellite observations and model simulated *TBs*, and the bias needs to be corrected in order to optimally merge the two types of data. For the computing efficiency, we employed mean-variance approach [56], [57], [58]. The correction is performed on a pixel-by-pixel basis by comparing the corresponding values of aggregated RSWAT *TB* simulations and SMAP observations. Furthermore, according to the SMAP algorithm documentation [44], we masked the regions with VWC greater than 5kg/m² before correction.

2) *Disaggregate SMAP TB Data to 30 m*: The Kalman filter method was utilized to disaggregate the SMAP *TB*, which can combine different types of observations at a single time step to find the optimal estimate of the corresponding state variable (i.e., SM). According to the Bayesian theory, the state variable can be expressed as [59]

$$\hat{X}_t = X_t + K \cdot (y_t - H \cdot X_t) \quad (7)$$

where t represents time, X_t and y_t are data from the model and observations, respectively, and \hat{X}_t represents the optimal estimate. K is the gain, which depends on the uncertainties of the model (P) and observations (R)

$$K = \frac{PH^T}{HPH^T + R} \quad (8)$$

where H is an observation operator, which maps system state space to observation space. T stands for transpose. Since this study was based on the pixel level, the scale and units of model and observed values are the same, so the value of H is 1.

The error in the model *TB* cannot be estimated directly and needs to be derived from the model SM error, where every 0.01 m³/m³ of SM error corresponds to 1 K of *TB* error [19]. In this study, the triple collocation method [60] was used to obtain the relative error between SMAP and RSWAT SM. As the accuracy requirement of SMAP SM is 0.04 m³/m³, the error in RSWAT SM can be deduced from the relative error, which further yields the error of RSWAT *TB*. The *TB* error of SMAP is 1.3 K [61], consequently, the P and R are the squares of the respective *TB* errors of RSWAT and SMAP. From (7) and (8), the Kalman filter method is a weighted averaging method, and its weight is determined by the relative magnitude of the uncertainty between the model and the observation.

Ultimately, with reference to (7), the formula for disaggregating the SMAP *TB* to 30 m is

$$\begin{aligned} \text{Disaggregated}_{TB} = & RSWAT_{TB} \\ & + K \cdot (SMAP_{TB} - RSWAT_{TB}). \end{aligned} \quad (9)$$

D. Retrieve SM at 30 m

Based on the 30 m disaggregated *TB*, we retrieved 30 m SM data by the *Tau-omega* model. The retrieval process adopted an iterative algorithm, which set the SM values at 0.01 intervals and then forward simulated the *TB* values. When the value of the least squares cost function between the simulated *TB* and

the disaggregated *TB* was the minimum, the corresponding SM value was the retrieval result.

IV. RESULTS AND DISCUSSIONS

A. RSWAT Simulated SM

Fig. 3 demonstrates the comparison between RSWAT SM and SWAT SM on the five measured sites. Compared to the original SWAT model, RSWAT effectively captures the dynamic changes of station SM, with less bias overall. Furthermore, Table II summarizes the calculated statistical metrics comprised of unbiased root mean square error (ubRMSE, m³/m³), RMSE (m³/m³), correlation coefficients (R), and bias (m³/m³) [62]. Overall, RSWAT outperforms SWAT in terms of RMSE, R, and Bias, except for ubRMSE, which is slightly worse, thus illustrating the effective improvement of RSWAT. Critically, RSWAT possesses the capability of simulating hourly SM.

Moreover, acknowledging the limitations of station validation, this study formed a triplet of RSWAT, SMAP, and ESA CCI active SM products, employing the triple collocation method to obtain the grid-scale error results, as displayed in Fig. 4. RSWAT denotes the lowest mean relative error (0.025 m³/m³), followed by SMAP (0.031 m³/m³), and active product exhibiting the largest (0.037 m³/m³), indicating the good capacity of RSWAT in simulating SM. Concurrently, by comparing IGBP types, it is observed that the accuracy of SMAP is low in forested areas, owing to vegetation cover disrupting microwave penetration [63]. However, RSWAT performed well in forest areas.

B. RSWAT Simulated TB

The 30 m RSWAT *TB* was simulated by the forward RTM based on the RSWAT SM data. We randomly selected a grid and analyzed the correlation between SMAP and RSWAT separately for *TB* and SM. As shown in Fig. 5, for *TB*, the R-squared between SMAP and RSWAT reached 0.81, which is significantly higher compared to the correlation for SM (0.20), the remaining grids followed similar pattern as the selected grid. This is because we used the same SCA-V algorithm as SMAP in the simulation of RSWAT *TB*. If the SM data from RSWAT and SMAP were directly combined, it would cause a large uncertainty. Therefore, this study chose to fuse *TB* rather than SM. In addition, the high correlation between SMAP and RSWAT *TB* satisfied the assumption of linearity between variables in Kalman filtering.

C. Gap Filling for High VWC Area

The SMAP (36 km) and RSWAT (30 m) *TB* were fused into a disaggregated *TB* at 30 m resolution, from which the SM was retrieved using the RTM. Consistent with the SMAP algorithm, we masked pixels with VWC > 5kg/m² [Fig. 6(a)], which mainly correspond to forest types in the SWAT land use data [FRSD, FRSE, and FRST in Fig. 6(b)]. Moreover, the water body (WATR) was excluded in the retrieval process. These two factors caused invalid pixels in the retrieval results [Fig. 6(c)]. For spatial integrity, we employed the mean-variance approach to remove the bias between RSWAT SM and SMAP SM. Invalid



Fig. 3. Simulated SM by SWAT and RSWAT at soil depth of 10 cm against stations.

pixels caused by the high VWC were filled by the matched RSWAT SM, resulting in a spatially continuous SM at 30 m [Merged SM, Fig. 6(d)] for spatial analysis. This reflects the strength of spatial integrity of the model data.

D. Spatiotemporal Variability of Merged SM

Fig. 7 reveals the spatiotemporal distribution of SM across different seasons in Lanjiang River Basin. For spatial distribution,

under the combined influence of topography, land use, and soil factors, the values of SM simulated by RSWAT show a pattern of lower in the middle and higher at the periphery. SMAP SM values have an extensive dynamic range. Moreover, SMAP has only 29 values within a watershed of nearly 20 000 km², which does not reflect the spatial heterogeneity of SM in the watershed and provides limited information. The merged SM captures the spatial pattern of RSWAT data and the magnitude pattern of SMAP data. Consequently, our proposed method well combines

TABLE II
MODEL PERFORMANCE COMPARISON BETWEEN SWAT AND RSWAT FOR SM AT FIVE IN-SITU STATIONS

Station	ubRMSE ($\text{m}^3 \cdot \text{m}^{-3}$)		RMSE ($\text{m}^3 \cdot \text{m}^{-3}$)		R		Bias ($\text{m}^3 \cdot \text{m}^{-3}$)	
	RSWAT	SWAT	RSWAT	SWAT	RSWAT	SWAT	RSWAT	SWAT
58547	0.055	0.069	0.211	0.350	0.689	0.485	-0.203	-0.343
K7399	0.041	0.038	0.083	0.152	0.669	0.642	-0.072	-0.147
K6601	0.049	0.057	0.084	0.063	0.691	0.417	0.068	0.026
K6603	0.042	0.022	0.197	0.137	0.644	0.697	0.193	0.136
K7121	0.070	0.033	0.077	0.101	0.219	0.477	-0.031	-0.095
Average	0.051	0.044	0.130	0.161	0.582	0.544	-0.009	-0.085

Bolded text indicates better performing indicators.

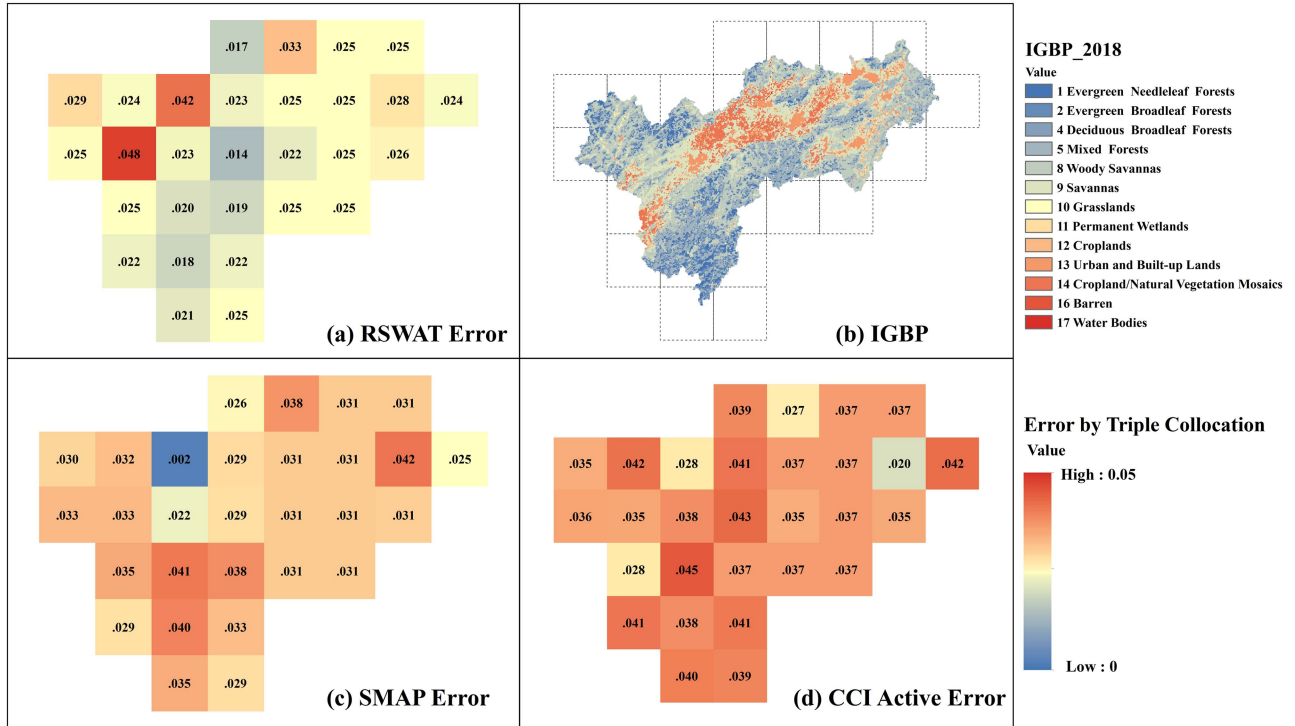


Fig. 4. Relative errors for RSWAT, SMAP, and CCI active SM product by triple collocation method.

the strengths of fine resolution of RSWAT and high precision of SMAP. The SM values are higher in forested areas and lower in other areas, which is consistent with the spatial distribution of land use [see Fig. 6(b)].

In terms of temporal variation, all three products exhibit similar trends and we selected four dates to represent seasonal variations. The highest value was found on April 26 due to increased precipitation in spring, followed by January 12 in winter and October 17 in autumn, and the lowest SM value was observed on July 15 in summer due to high temperature and evaporation.

To investigate the SM distribution in detail, Fig. 8 enlarges a 36 km SMAP grid (red box) in Fig. 7. Compared to the single value of the SMAP grid, the RSWAT model captures the spatial variation of SM. In addition, because of the integration of spatial information from RSWAT and SMAP data, the merged SM is more refined, thus making the spatial heterogeneity of the SM more apparent. Therefore, our method provides spatial

variability of SM within and among fields, which benefits the planning of irrigation and fertilization.

E. Comparative Analysis

1) *Relevance to the SMAP Official SM Products:* Fig. 9(a) and (b) shows the correlations between disaggregated SM and SMAP 9 and 36 km SM products, respectively. Since the resolutions of the three products are different, we took the SMAP at intermediate 9 km grid as the benchmark for correlation analysis. There are good correlations between disaggregated SM and SMAP SM products at different scales. Correlation values follow the spatial distribution characteristics of IGBP land cover [see Fig. 9(c)]. In nonforested areas, correlations are high. The average correlation between the disaggregated SM product and the 9 km product is 0.73, and the average correlation with the 36 km product is 0.75. In certain grids, the correlation reaches values of 0.8 or even higher, up to 0.9. On the contrary, weak

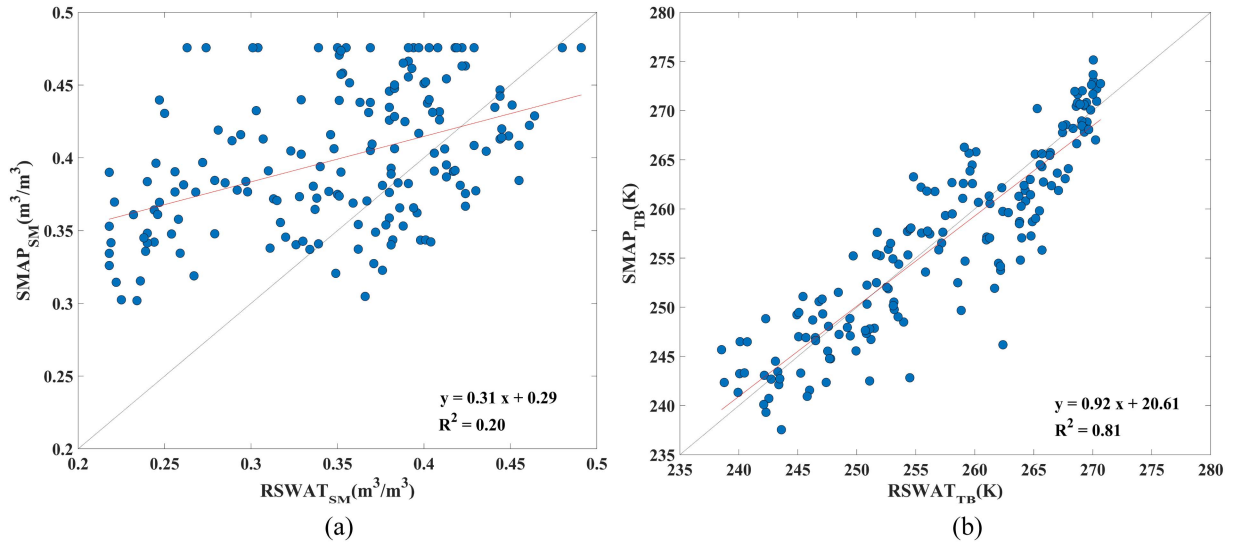


Fig. 5. Scatterplot of (a) RSWAT simulated SM with SMAP SM products, and (b) RSWAT simulated TB using *Tau-omega* model with SMAP TB.

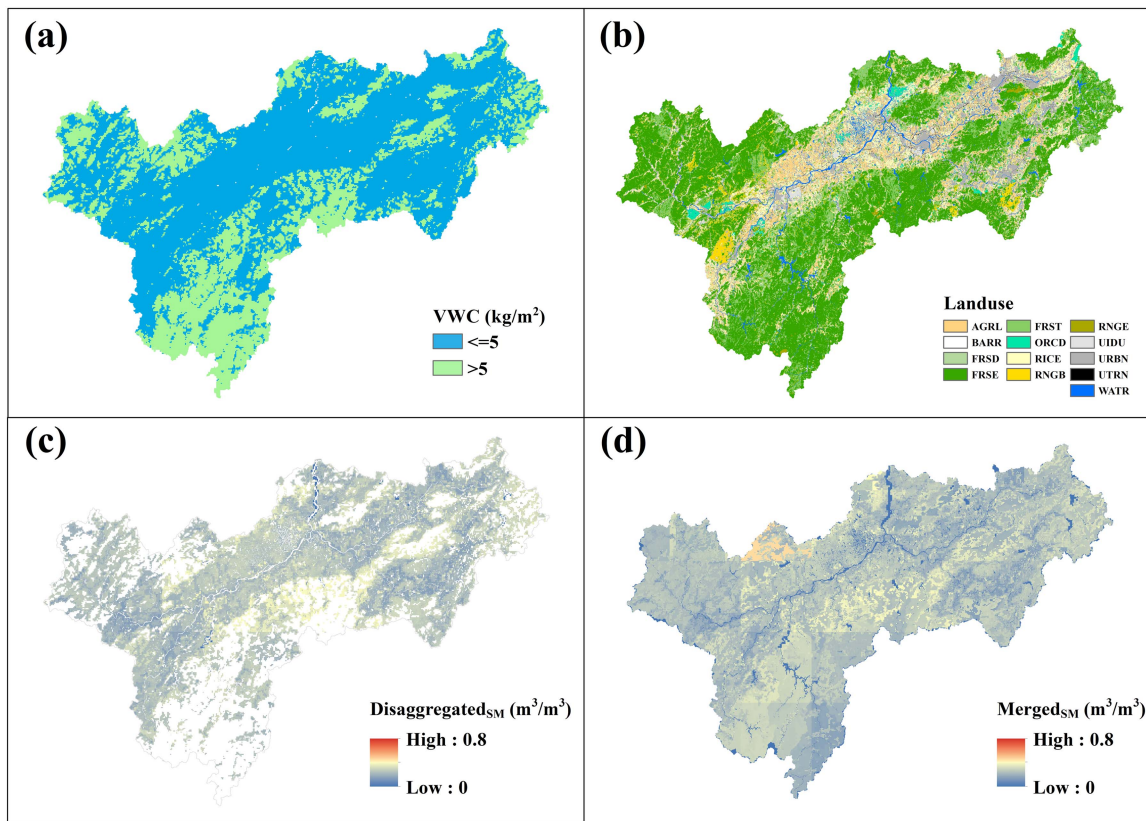


Fig. 6. Spatial distribution of (a) VWC, (b) land use in SWAT simulation, (c) disaggregated SM, and (d) merged SM in Lanjiang River Basin (July 15, 2018).

correlations are found in forested areas due to high retrieval uncertainty caused by strong attenuation and scattering effects from the dense canopy. The overall strong correlation with the SMAP official products indicates a robust performance of our product in capturing the variability of SM.

2) *Comparison of Statistical Metrics With Multiple SMAP Products:* Fig. 10 exhibits the statistical metrics for disaggregated SM and five SMAP SM products (SMAP 9 km, SMAP 36 km, SMAP MCCA, SMAP MT-DCA, and SMAP-IB) against the *in-situ* measurements (see Fig. 1).

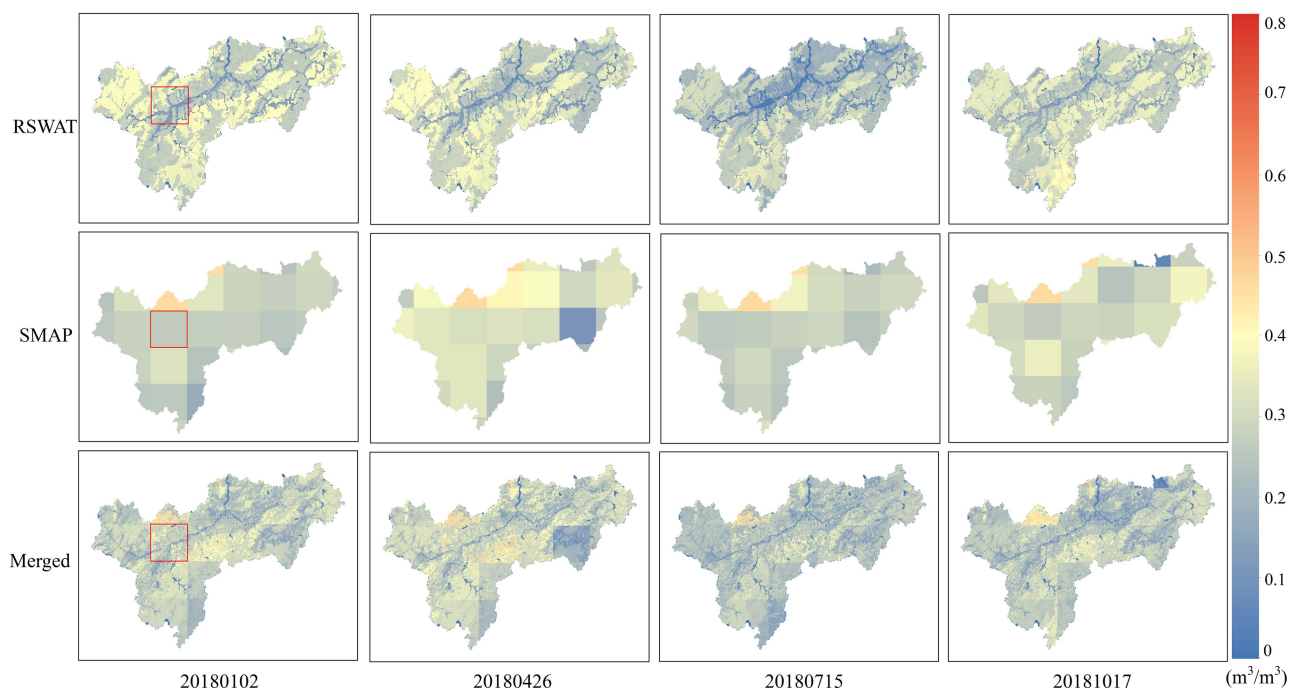


Fig. 7. Overall spatiotemporal distribution of RSWAT, SMAP, and the merged SM.

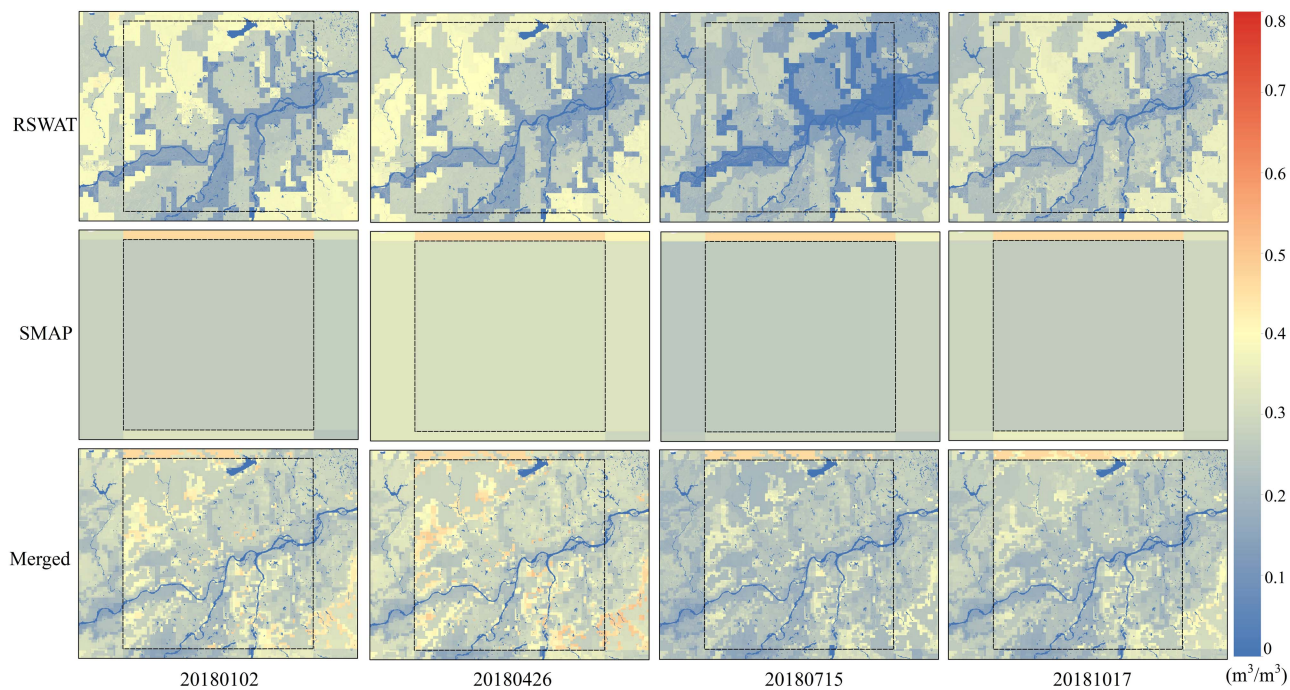


Fig. 8. Comparison of spatiotemporal distribution among RSWAT, SMAP, and the merged SM at grid scale.

For ubRMSE, the disaggregated product has the highest precision (average value is $0.042 \text{ m}^3/\text{m}^3$), which indicates that our products have satisfactory accuracy. For RMSE, apart from the SMAP-IB product, there was little difference between the other products. Among them, the disaggregated product outperforms the rest (average value is $0.064 \text{ m}^3/\text{m}^3$). The RMSE of SMAP-IB

product was much larger than the other products, which may be due to the effect of soil temperature. It used ERA-Interim soil temperature data from the European Centre for Medium-Range Weather Forecasts, whereas soil temperatures for all other SMAP products were obtained from the Goddard Earth Observing System 5.

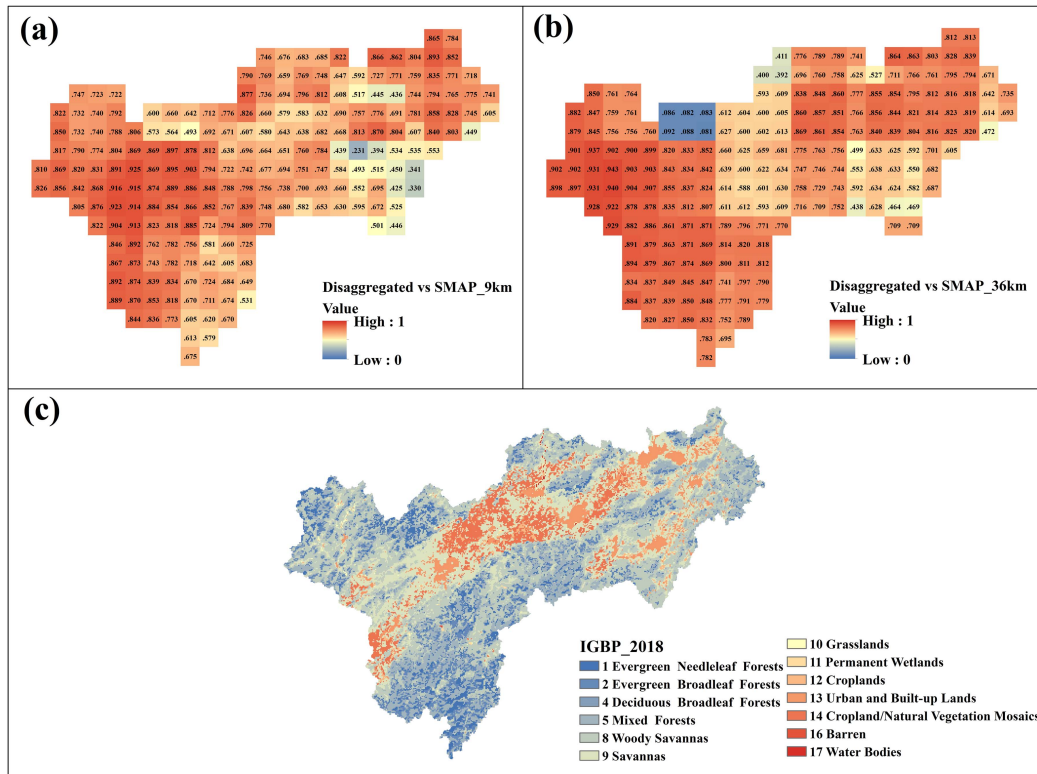


Fig. 9. (a) Correlations of disaggregated SM with SMAP 9 km products. (b) Correlations of disaggregated SM with SMAP 36 km products. (c) MODIS IGBP land cover type in Lanjiang River Basin.

Regarding correlation, MT-DCA ranks first (average value is 0.492), closely followed by the disaggregated product (average value is 0.435). However, the average correlations of all products are not particularly high. This may be due to the fact that the range of moisture variation at certain individual sites (K7121 and K6603) throughout the year does not exceed $0.1 \text{ m}^3/\text{m}^3$ (see Fig. 3), which is relatively small, so it is difficult for the products to fully capture the dynamic changes in SM. The poor R performance of the products with a small range of dynamic variation was also found by Ma et al. [63] and Burgin et al. [64]. In terms of bias, SMAP-IB has the largest bias, probably due to the larger bias in the soil temperature product.

Overall, the disaggregated products had the highest precision and a satisfactory level of correlation and bias.

F. Uncertainty Analysis

Although this study provided high spatial resolution SM products with promising application prospects, there are still limitations. We analyzed the uncertainties of this study from the following three aspects:

1) *Uncertainty in SWAT Model Simulation:* DEM, land use, and soil data are the input data to the SWAT model. The DEM and land use data used in this study have a spatial resolution of 30 m, whereas the soil data have a spatial resolution of 1 km. Although HWSD is widely used in the SWAT model, future work is needed to compare the applicability of finer soil data (e.g., SoilGrids data at 250 m) in the SWAT model.

Furthermore, the SWAT model is a semiempirical and semi-physical model where many elements of the calculation process are parameterized. The default parameters in the SWAT model were obtained based on geographical conditions in the USA, which may deviate from the soil and vegetation conditions at our study sites.

Another major source of uncertainty is human activities, such as irrigation and groundwater extraction, which significantly affect the SM at the field scale [19]. There is a water management module in SWAT that can be used in future studies to investigate the impact of human activities on SM.

2) *Uncertainty in RTM Model:* The uncertainty in RTM is mainly caused by the auxiliary data. For instance, the clay content of the soil was involved in the Mironov dielectric model, so the soil data impacted the uncertainty in the forward simulation of TB. In addition, the vegetation optical thickness, roughness, and single scattering albedo in the RTM are parameterized according to MODIS IGBP land cover types. For example, in this study, we set the roughness, albedo, and *stem-factor* of grassland as constants 0.156, 0.05, and 1.5, respectively. Therefore, the accuracy of IGBP data and the rationality of the parameterization also affect the uncertainty of the model [65]. In particular, the reasonable values of optical parameter for different regions should be explored. Similarly, the auxiliary data also has the problem of scale mismatch, and it is necessary to investigate other high spatial resolution auxiliary data.

3) *Uncertainty in Disaggregation and Validation Methods:* Regarding the Kalman filter algorithm, the determination of

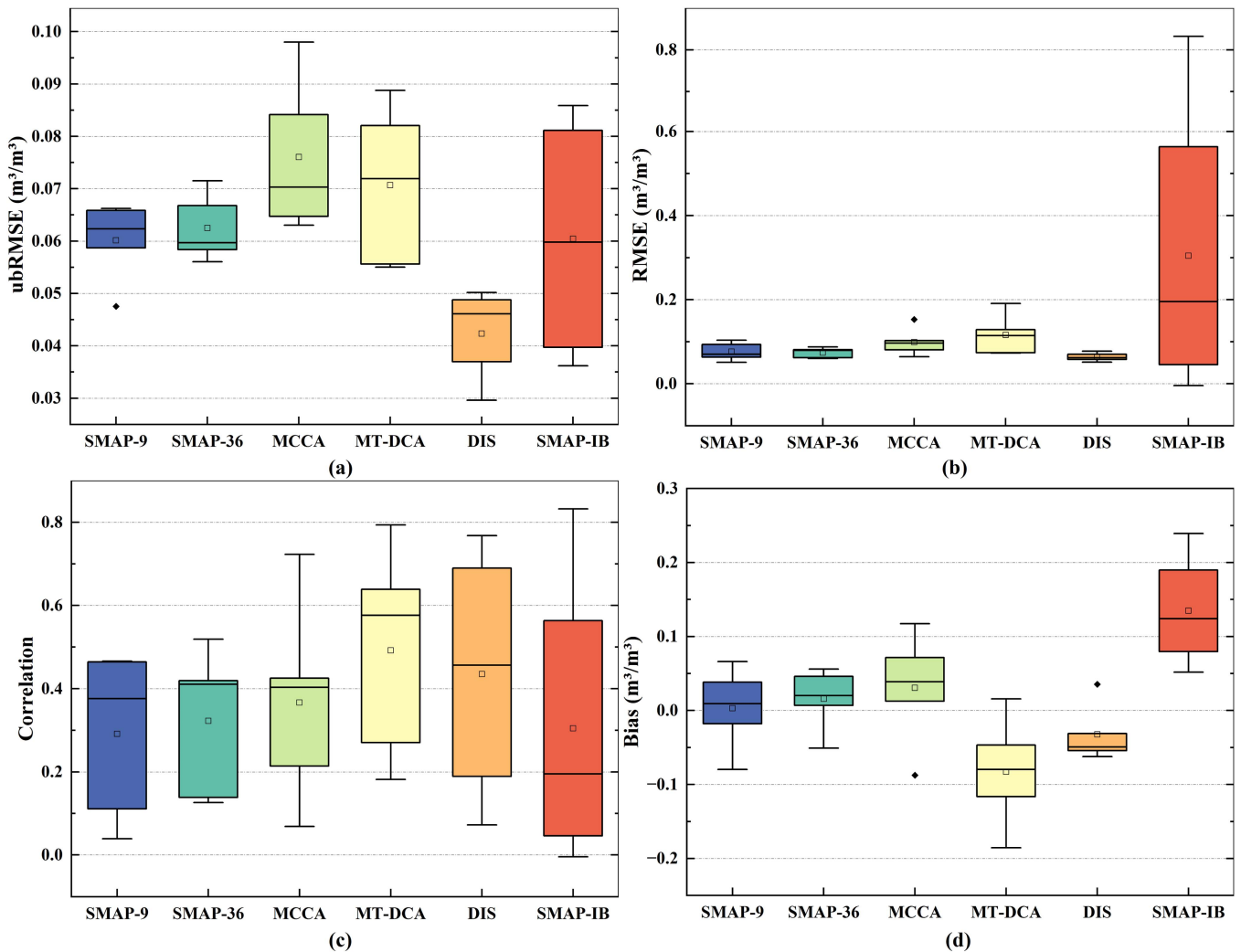


Fig. 10. Boxplots of the performance metrics (ubRMSE, RMSE, Correlation, and Bias) of disaggregated (DIS), SMAP 9 km, 36 km, MCCA, MT-DCA, and SMAP-IB SM products.

P and R is based on previous research [61], [66]. Although this study used triple collocation approach to spatially quantify the values of P and R for different grids, there is also temporal variability in the errors of the products, thus the time-varying values of P and R should be considered in future studies.

For product validation, the quality evaluation of high-resolution SM is challenging. We will compare traditional validation metrics with other evaluation criteria, such as those proposed by Crow et al. [67] and Merlin et al. [68] in future studies to investigate the performance of our products under different criteria.

V. CONCLUSION

This article proposed a coupling process with a physical mechanism to retrieve SM at 30 m spatial resolution, by integrating the SWAT hydrological model with *Tau-Omega* RTM. First, a modified SWAT model integrating a physically based SM module was applied, which is more accurate and less biased

compared to the SM simulated by the original SWAT model. Subsequently, the added values of the modified SWAT model were combined with SMAP *TB* data. The quality of SMAP *TB* data is relatively high, but it has coarse resolution. In contrast, the high spatial resolution SWAT *TB* data can capture spatial heterogeneity in detail within a SMAP grid. Thus, combining these two observations allows the SMAP *TB* to be disaggregated from coarse to fine spatial resolution. Ultimately, this study yielded SM retrievals with high spatial resolution as SWAT and high precision as SMAP.

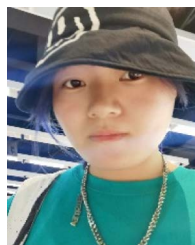
Additionally, in forested areas, the penetration of microwave signals is very limited, which leads to inaccurate results. We filled these areas with the SM from SWAT model, reflecting the advantage of the hydrological model with spatiotemporal continuity.

The method presented in this study has important implications for precision agriculture, field-scale water management, and further improvement of hydrological and land surface models. In the upcoming studies, we will explore more effective methods for SM retrieval in forested areas.

REFERENCES

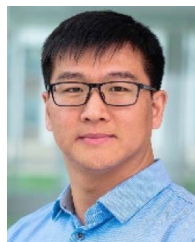
- [1] C. Dang et al., "Assessment of the importance of increasing temperature and decreasing soil moisture on global ecosystem productivity using solar-induced chlorophyll fluorescence," *Glob. Change Biol.*, vol. 28, no. 6, pp. 2066–2080, 2022.
- [2] Z. Fu et al., "Uncovering the critical soil moisture thresholds of plant water stress for European ecosystems," *Glob. Change Biol.*, vol. 3, no. 6, pp. 2111–2123, 2022.
- [3] L. Liu, L. Gudmundsson, M. Hauser, D. Qin, S. Li, and S. I. Seneviratne, "Soil moisture dominates dryness stress on ecosystem production globally," *Nature Commun.*, vol. 11, no. 1, pp. 1–9, 2020.
- [4] V. Humphrey et al., "Soil moisture–atmosphere feedback dominates land carbon uptake variability," *Nature*, vol. 592, pp. 65–69, 2021.
- [5] E. Jalilvand, R. Abolafia-Rosenzweig, M. Tajrishy, and N. Das, "Evaluation of SMAP/Sentinel 1 high-resolution soil moisture data to detect irrigation over agricultural domain," *IEEE J. Sel. Topics Appl. Earth Observ. Remote Sens.*, vol. 14, pp. 10733–10747, 2021.
- [6] H. Lievens et al., "Joint Sentinel-1 and SMAP data assimilation to improve soil moisture estimates," *Geophys. Res. Lett.*, vol. 44, no. 12, pp. 6145–6153, 2017.
- [7] E. Seo, M. I. Lee, and R. H. Reichle, "Assimilation of SMAP and ASCAT soil moisture retrievals into the JULES land surface model using the local ensemble transform Kalman filter," *Remote Sens. Environ.*, vol. 253, 2021, Art. no. 112222.
- [8] F. T. Ulaby, R. K. Moore, and A. K. Fung, *Microwave Remote Sensing: Active and Passive, Volume II: Radar Remote Sensing and Surface Scattering and Emission Theory*. Norwood, MA, USA: Addison-Wesley, 1982.
- [9] T. Zhao, "Recent advances of L-band application in the passive microwave remote sensing of soil moisture and its prospects," *Prog. Geography*, vol. 37, no. 2, pp. 198–213, 2018.
- [10] Y. H. Kerr et al., "The SMOS mission: New tool for monitoring key elements of the global water cycle," *Proc. IEEE*, vol. 98, no. 5, pp. 666–687, May 2010.
- [11] D. Entekhabi et al., "The soil moisture active/passive mission (SMAP)," in *Proc. IEEE Int. Geosci. Remote Sens. Symp.*, 2010, vol. 98, pp. 704–716.
- [12] J. P. Wigneron et al., "Modelling the passive microwave signature from land surfaces: A review of recent results and application to the L-band SMOS & SMAP soil moisture retrieval algorithms," *Remote Sens. Environ.*, vol. 192, pp. 238–262, 2017.
- [13] T. Zhao et al., "Soil moisture experiment in the Luan River supporting new satellite mission opportunities," *Remote Sens. Environ.*, vol. 240, 2020, Art. no. 111680.
- [14] J. Peng, A. Loew, O. Merlin, and N. E. C. Verhoest, "A review of spatial downscaling of satellite remotely sensed soil moisture," *Rev. Geophys.*, vol. 55, no. 2, pp. 341–366, 2017.
- [15] N. N. Das, D. Entekhabi, and E. G. Njoku, "An algorithm for merging SMAP radiometer and radar data for high-resolution soil-moisture retrieval," *IEEE Trans. Geosci. Remote Sens.*, vol. 49, no. 5, pp. 1504–1512, May 2011.
- [16] J. Kang, R. Jin, X. Li, C. Ma, J. Qin, and Y. Zhang, "High spatio-temporal resolution mapping of soil moisture by integrating wireless sensor network observations and MODIS apparent thermal inertia in the Babao River Basin, China," *Remote Sens. Environ.*, vol. 191, pp. 232–245, 2017.
- [17] K. J. Ranney, J. D. Niemann, B. M. Lehman, T. R. Green, and A. S. Jones, "A method to downscale soil moisture to fine resolutions using topographic, vegetation, and soil data," *Adv. Water Resour.*, vol. 76, pp. 81–96, 2015.
- [18] G. Kim and A. P. Barros, "Downscaling of remotely sensed soil moisture with a modified fractal interpolation method using contraction mapping and ancillary data," *Remote Sens. Environ.*, vol. 83, no. 3, pp. 400–413, 2002.
- [19] N. Vergopolan et al., "Combining hyper-resolution land surface modeling with SMAP brightness temperatures to obtain 30-m soil moisture estimates," *Remote Sens. Environ.*, vol. 242, 2020, Art. no. 111740.
- [20] T. Ma, Z. Duan, R. Li, and X. Song, "Enhancing SWAT with remotely sensed LAI for improved modelling of ecohydrological process in subtropics," *J. Hydrol.*, vol. 570, pp. 802–815, 2019.
- [21] S. Pang, X. Wang, C. S. Melching, and K. H. Feger, "Development and testing of a modified SWAT model based on slope condition and precipitation intensity," *J. Hydrol.*, vol. 588, 2020, Art. no. 125098.
- [22] A. Patil and R. A. A. J. Ramsankaran, "Improving streamflow simulations and forecasting performance of SWAT model by assimilating remotely sensed soil moisture observations," *J. Hydrol.*, vol. 555, pp. 683–696, 2017.
- [23] M. A. Rajib, V. Merwade, and Z. Yu, "Multi-objective calibration of a hydrologic model using spatially distributed remotely sensed/in-situ soil moisture," *J. Hydrol.*, vol. 536, pp. 192–207, 2016.
- [24] L. Sun, O. Seidou, I. Nistor, K. Goita, and R. Magagi, "Simultaneous assimilation of in situ soil moisture and streamflow in the SWAT model using the extended Kalman filter," *J. Hydrol.*, vol. 543, pp. 671–685, 2016.
- [25] B. Narasimhan, R. Srinivasan, J. G. Arnold, and M. D. Luzio, "Estimation of long-term soil moisture using a distributed parameter hydrologic model and verification using remotely sensed data," *Trans. ASAE Amer. Soc. Agricultural Engineers*, vol. 48, no. 3, pp. 1101–1113, 2005.
- [26] A. G. Mengistu, Y. E. Woyessa, L. D. van Rensburg, and W. A. Tesfahuney, "Analysis of the spatio-temporal variability of soil water dynamics in an arid catchment in South Africa," *Geoderma Regional*, vol. 25, 2021, Art. no. e00395.
- [27] S. B. Havrylenko, J. M. Bodoque del Pozo, R. Srinivasan, G. V. Zucarelli, and P. Mercuri, "Assessment of the soil water content in the Pampas region using SWAT," *Catena*, vol. 137, pp. 298–309, 2016.
- [28] M. X. Li, Z. G. Ma, and J. W. Du, "Regional soil moisture simulation for Shaanxi Province using SWAT model validation and trend analysis," *Sci. China Earth Sci.*, vol. 53, no. 4, pp. 575–590, 2010.
- [29] Y. Luo, C. He, M. Sophocleous, Z. Yin, R. Hongrui, and Z. Ouyang, "Assessment of crop growth and soil water modules in SWAT2000 using extensive field experiment data in an irrigation district of the Yellow River Basin," *J. Hydrol.*, vol. 352, no. 1/2, pp. 139–156, 2008.
- [30] J. Qi et al., "Assessing the performance of a physically-based soil moisture module integrated within the soil and water assessment tool," *Environ. Model. Softw.*, vol. 109, pp. 329–341, 2018.
- [31] W. Chen, C. Huang, Z.-L. Yang, and Y. Zhang, "Retrieving accurate soil moisture over the Tibetan Plateau using multi-source remote sensing data assimilation with simultaneous state and parameter estimations," *J. Hydrometeorol.*, vol. 22, pp. 2751–2766, 2021.
- [32] G. J. M. D. Lannoy and R. H. Reichle, "Global assimilation of multiangle and multipolarization SMOS brightness temperature observations into the GEOS-5 catchment land surface model for soil moisture estimation," *J. Hydrometeorol.*, vol. 17, no. 2, pp. 669–691, 2016.
- [33] T. Mo, B. J. Choudhury, T. J. Schumge, J. R. Wang, and T. J. Jackson, "A model for microwave emission from vegetation-covered fields," *J. Geophys. Res.*, vol. 87, no. C13, pp. 11229–11237, 1982.
- [34] B. Fang, V. Lakshmi, R. Bindlish, and T. J. Jackson, "Downscaling of SMAP soil moisture using land surface temperature and vegetation data," *Vadose Zone J.*, vol. 17, no. 1, pp. 1–15, 2018.
- [35] J. Zheng et al., "Soil moisture downscaling using multiple modes of the DISPATCH algorithm in a semi-humid/humid region," *Int. J. Appl. Earth Observ. Geoinf.*, vol. 104, 2021, Art. no. 102530.
- [36] Z. Wei, Y. Meng, W. Zhang, J. Peng, and L. Meng, "Downscaling SMAP soil moisture estimation with gradient boosting decision tree regression over the Tibetan Plateau," *Remote Sens. Environ.*, vol. 225, pp. 30–44, 2019.
- [37] L. Liu, C. Gao, W. Xuan, and Y. P. Xu, "Evaluation of medium-range ensemble flood forecasting based on calibration strategies and ensemble methods in Lanjiang Basin, Southeast China," *J. Hydrol.*, vol. 554, pp. 233–250, 2017.
- [38] A. Jarvis, J. Rubiano, A. Nelson, A. Farrow, and M. Mulligan, "Practical use of SRTM data in the tropics: Comparisons with digital elevation models generated from cartographic data," Centro Internacional de Agricultura Tropical, Cali, Colombia, 2004.
- [39] FAO, "Harmonized world soil database (version 1.2)," Food and Agriculture Organization, 2009, Accessed: Aug. 17, 2023. [Online]. Available: <http://www.fao.org/soils-portal/soil-survey/soil-maps-and-databases/harmonized-world-soil-database-v12/en/>
- [40] C. S. Draper, J. P. Walker, P. J. Steinle, R. A. M. de Jeu, and T. R. H. Holmes, "An evaluation of AMSR-E derived soil moisture over Australia," *Remote Sens. Environ.*, vol. 113, no. 4, pp. 703–710, 2009.
- [41] F. Chen et al., "Global-scale evaluation of SMAP, SMOS and ASCAT soil moisture products using triple collocation," *Remote Sens. Environ.*, vol. 214, pp. 1–13, 2018.
- [42] T. J. Jackson, "Measuring surface soil moisture using passive microwave remote sensing," *Hydrol. Processes*, vol. 7, no. 2, pp. 139–152, 1993.

- [43] C. Ma, X. Li, J. Wang, C. Wang, Q. Duan, and W. Wang, "A comprehensive evaluation of microwave emissivity and brightness temperature sensitivities to soil parameters using qualitative and quantitative sensitivity analyses," *IEEE Trans. Geosci. Remote Sens.*, vol. 55, no. 2, pp. 1025–1038, Feb. 2017.
- [44] P. O'Neill et al., "Soil Moisture Active Passive (SMAP): Algorithm theoretical basis document level 2 & 3 soil moisture (passive) data products," Jet Propulsion Lab., California Inst. Technol., Pasadena, CA, USA, 2021.
- [45] T. Zhao et al., "Retrievals of soil moisture and vegetation optical depth using a multi-channel collaborative algorithm," *Remote Sens. Environ.*, vol. 257, 2021, Art. no. 112321.
- [46] A. G. Konings, M. Piles, N. Das, and D. Entekhabi, "L-band vegetation optical depth and effective scattering albedo estimation from SMAP," *Remote Sens. Environ.*, vol. 198, pp. 460–470, 2017.
- [47] X. Li et al., "A new SMAP soil moisture and vegetation optical depth product (SMAP-IB): Algorithm, assessment and inter-comparison," *Remote Sens. Environ.*, vol. 271, 2022, Art. no. 112921.
- [48] J. Chaubell et al., "Backus-Gilbert optimal interpolation applied to enhance SMAP data: Implementation and assessment," in *Proc. IEEE Int. Geosci. Remote Sens. Symp.*, 2017, pp. 2531–2534.
- [49] A. Colliander et al., "Validation of soil moisture data products from the NASA SMAP mission," *IEEE J. Sel. Topics Appl. Earth Observ. Remote Sens.*, vol. 15, pp. 364–392, 2022.
- [50] W. Dorigo et al., "ESA CCI soil moisture for improved earth system understanding: State-of-the art and future directions," *Remote Sens. Environ.*, vol. 203, pp. 185–215, 2017.
- [51] S. L. Neitsch, J. G. Arnold, J. R. Kiniry, and J. R. Williams, "Soil & water assessment tool theoretical documentation version 2009," Texas Water Resour. Inst., Texas A&M Univ. Syst., College Station, TX, USA, Tech. Rep. 406, 2011.
- [52] T. J. Jackson and T. J. Schmugge, "Vegetation effects on the microwave emission of soils," *Remote Sens. Environ.*, vol. 36, no. 3, pp. 203–212, 1991.
- [53] V. L. Mironov, L. G. Kosolapova, and S. V. Fomin, "Physically and mineralogically based spectroscopic dielectric model for moist soils," *IEEE Trans. Geosci. Remote Sens.*, vol. 47, no. 7, pp. 2059–2070, Jul. 2009.
- [54] F. T. Ulaby, R. K. Moore, and A. K. Fung, *Microwave Remote Sensing: Active and Passive. Volume I: Microwave Remote Sensing Fundamentals and Radiometry*. Norwood, MA, USA: Addison-Wesley, 1981.
- [55] J.-P. Wigneron, L. Laguerre, and Y. H. Kerr, "A simple parameterization of the L-band microwave emission from rough agricultural soils," *IEEE Trans. Geosci. Remote Sens.*, vol. 39, no. 8, pp. 1697–1707, Aug. 2001.
- [56] C. Massari, L. Brocca, A. Tarpanelli, and T. Moramarco, "Data assimilation of satellite soil moisture into rainfall-runoff modelling: A complex recipe?," *Remote Sens.*, vol. 7, no. 9, pp. 11403–11433, 2015.
- [57] H. Lievens et al., "SMOS soil moisture assimilation for improved hydrologic simulation in the Murray Darling Basin, Australia," *Remote Sens. Environ.*, vol. 168, pp. 146–162, 2015.
- [58] D. Long et al., "Generation of MODIS-like land surface temperatures under all-weather conditions based on a data fusion approach," *Remote Sens. Environ.*, vol. 246, 2020, Art. no. 111863.
- [59] R. G. Brown and P. Y. C. Hwang, *Introduction to Random Signals and Applied Kalman Filtering: With MATLAB Exercises and Solutions*, 3rd ed. Hoboken, NJ, USA: Wiley, 1996.
- [60] K. Scipal, W. Dorigo, and R. deJeu, "Triple collocation—A new tool to determine the error structure of global soil moisture products," in *Proc. IEEE Int. Geosci. Remote Sens. Symp.*, 2010, pp. 4426–4429.
- [61] J. R. Piepmeier et al., "SMAP L-band microwave radiometer: Instrument design and first year on orbit," *IEEE Trans. Geosci. Remote Sens.*, vol. 55, no. 4, pp. 1954–1966, Apr. 2017.
- [62] D. Entekhabi, R. H. Reichle, R. D. Koster, and W. T. Crow, "Performance metrics for soil moisture retrievals and application requirements," *J. Hydrometeorol.*, vol. 11, no. 3, pp. 832–840, 2010.
- [63] H. Ma et al., "An assessment of L-band surface soil moisture products from SMOS and SMAP in the tropical areas," *Remote Sens. Environ.*, vol. 284, no. 113344, 2023.
- [64] M. S. Burgin et al., "A comparative study of the SMAP passive soil moisture product with existing satellite-based soil moisture products," *IEEE Trans. Geosci. Remote Sens.*, vol. 55, no. 5, pp. 2959–2971, May 2017.
- [65] J. Zeng, K.-S. Chen, H. Bi, and Q. Chen, "A preliminary evaluation of the SMAP radiometer soil moisture product over United States and Europe using ground-based measurements," *IEEE Trans. Geosci. Remote Sens.*, vol. 54, no. 8, pp. 4929–4940, Aug. 2016.
- [66] D. Entekhabi, "SMAP handbook. Soil moisture active passive," Jet Propulsion Lab., California Inst. Technol., Pasadena, CA, USA, JPL 400-1567, 2014. [Online]. Available: https://smap.jpl.nasa.gov/files/smap2/SMAP_Handbook_FINAL_1_JULY_2014_Web.pdf
- [67] W. T. Crow, F. Chen, and A. Colliander, "Benchmarking downscaled satellite-based soil moisture products using sparse, point-scale ground observations," *Remote Sens. Environ.*, vol. 283, 2022, Art. no. 113300.
- [68] O. Merlin et al., "Performance metrics for soil moisture downscaling methods: Application to DISPATCH data in Central Morocco," *Remote Sens.*, vol. 7, no. 4, pp. 3783–3807, 2015.



Luyao Zhu received the B.Sc. degree from Anhui Normal University, Wuhu, China, in 2016. She is currently working toward the Ph.D. degree in agricultural remote sensing with the Department of Environment and Resource Science, Zhejiang University, Hangzhou, China.

Her research interests include microwave soil moisture retrieval, multisource data fusion, and assimilation of remote sensing data into hydrological models.



Junyu Qi received the B.E. degree in hydrology and water resources engineering from China University of Geosciences, Beijing, China, in 2007, the M.S. degree in physical geography from the Chinese Academy of Sciences, Beijing, China, in 2010, and the Ph.D. degree in forestry and environmental management from the University of New Brunswick, Fredericton, NB, Canada, in 2017.

He was a Postdoctoral Research Associate with the Earth System Science Interdisciplinary Center (ESSIC), University of Maryland, College Park, MD, USA.

Since 2020, he has been an Assistant/Associate Research Scientist within ESSIC. He is the PI for multiple projects, which include the NASA Carbon Monitoring System, NASA Carbon Cycle Science, and the USDA-NIFA Foundational and Applied Science Program. His main research emphasizes on uncovering the interconnections between climate, landscape, and hydrological and biogeochemical processes of complex ecosystem systems using physical, mathematical, and biological modeling approaches.



Hongquan Wang received the B.Sc. degree in geographic information systems from the Northeast Forestry University, Harbin, China, in 2007, the M.Sc. degree in silviculture (forest remote sensing) from the Chinese Academy of Forestry, Beijing, China, in 2010, and the Ph.D. degree in synthetic aperture radar remote sensing from the National Institute of Applied Sciences, IETR CNRS-6164, Rennes, France, in 2014.

He was involved in several scientific projects in the framework of CNRS Zone Atelier Armorique in France. From 2014 to 2018, he was a Postdoctoral Fellow with the Center for Research and Application of Remote Sensing, University of Sherbrooke, Sherbrooke, QC, Canada, where he participated in the Soil Moisture Active Passive Validation Experiments in 2012 and 2016. From 2018 to 2021, he was an Assistant Professor with the Department of Environment and Resource Science, Zhejiang University, Hangzhou, China. As a Principal Investigator, he led several research programs to develop remote sensing models, algorithms, and applications to characterize hydrosphere, cryosphere, biosphere, ecosystem, and climate changes. Since 2021, he has been a Researcher with the University of Sherbrooke and then at the Agriculture and Agri-Food Canada. His research interests include the development of multisource remote sensing (radar, radiometer, multispectral, hyperspectral, lidar) methodologies (e.g., polarimetric decompositions, radiative transfer models) and applications to characterize the dynamics of the earth system.



Mengmeng Zhou received the Ph.D. degree in agronomy from Zhejiang University, Hangzhou, China, in 2022.

In 2022, she joined Changzhou University, Changzhou, China, as a Lecturer. She is mainly engaged in the research of remote sensing survey and assessment of ecological environment, ecosystem service value assessment, ecological protection area planning and other directions, and has authored/coauthored articles in SCI journals such as *Science of the Total Environment* and *Journal of Cleaner Production*. She has participated in a number of horizontal projects, such as “Delineation of Ecological Protection Red Line (Tonglu County)” and “Assessment of Ecosystem Patterns and Functions in Zhejiang Province (2010–2015)”.



Xiaodong Deng received the B.Sc. degree in surveying and mapping engineering and M.Sc. degree in geodesy from Guizhou University, Guiyang, China, in 2012 and 2016, respectively. He is currently working toward the Ph.D. degree in agricultural remote sensing with the Institute of Applied Remote Sensing and Information Technology, College of Environmental and Resource Sciences, Zhejiang University, Hangzhou, China.

His research interests include microwave remote sensing of soil and Global Navigation Satellite System Reflectometry applications.



Yang Ye received the B.S. degree in hydraulic and hydropower engineering from Dalian University of Technology, Dalian, China, in 2015, the M.S. degree in civil engineering from the National Taiwan University, New Taipei, Taiwan, in 2017, and the Ph.D. degree in agricultural remote sensing from the Institute of Applied Remote Sensing and Information Technology, College of Environmental and Resource Sciences, Zhejiang University, Hangzhou, China, in 2022.

Her research interests include nighttime light remote sensing, sustainable development, and image processing.



Shan He received the B.Sc. degree in agricultural resources and environment from Shandong Agricultural University, Tai'an, China, in 2014, and the Ph.D. degree in agricultural remote sensing from the Institute of Applied Remote Sensing and Information Technology, College of Environmental and Resource Sciences, Zhejiang University, Hangzhou, China, in 2019.

She is currently with the Department of Economics and Management, China Jiliang University, Hangzhou, China. Her research interests include land resources management and Big Data mining.



Yongjun Li received the B.Sc. degree in landscape architecture from Nanjing Agricultural University, Nanjing, China, in 2017, and the Ph.D. degree in agricultural remote sensing from Zhejiang University, Hangzhou, China, in 2023.

She is a Research Assistant with Nanjing Agricultural University. She was involved in a number of scientific programs including National Natural Science Foundation of China and Open Fund of Key Laboratory of Urban Land Resources Monitoring and Simulation, Ministry of Natural Resources, China.

Her research interests include ecosystem services and landscape preferences.



Ke Wang (Member, IEEE) received the Ph.D. degree in soil chemistry from Zhejiang University, Hangzhou, China, in 1992.

He is currently a Professor with Zhejiang University. His research interests include land-use planning and management, digital agriculture, and geographic information system.



Cheng Tong received the B.Sc. degree in geographic information science from Anhui University of Science and Technology, Huainan, China, in 2017. He is currently working toward the Ph.D. degree in agricultural remote sensing with the Institute of Applied Remote Sensing and Information Technology, College of Environmental and Resource Sciences, Zhejiang University, Hangzhou, China.

His research interests include active and passive microwave remote sensing of soil moisture and nighttime light remote sensing.